Published in final edited form as:

Phys Med Biol. 2016 December 07; 61(23): 8321–8339. doi:10.1088/0031-9155/61/23/8321.

Loss of gas from echogenic liposomes exposed to pulsed ultrasound

Jason L. Raymond[1,a,b], **Ying Luan**[2], **Tao Peng**[3], **Shao-Ling Huang**[3], **David D. McPherson**[3], **Michel Versluis**[4], **Nico de Jong**[2], and **Christy K. Holland**[1,5]

[1]Biomedical Engineering Program, University of Cincinnati, Cardiovascular Center 3940, 231 Albert Sabin Way, Cincinnati, Ohio 45267-0586 [2]Department of Biomedical Engineering, Thoraxcenter, Erasmus Medical Center, P.O. Box 2040, 3000 CA, Rotterdam, Netherlands [3]Department of Internal Medicine, Division of Cardiology, University of Texas Health Science Center, Houston, Texas [4]Physics of Fluids Group, MIRA Institute for Biomedical Technology and Technical Medicine, University of Twente, P.O. Box 217, 7500 AE, Enschede, Netherlands [5]Department of Internal Medicine, Division of Cardiovascular Health and Disease, University of Cincinnati, Cardiovascular Center 3935, 231 Albert Sabin Way, Cincinnati, Ohio 45267-0586

Abstract

The destruction of echogenic liposomes (ELIP) in response to pulsed ultrasound excitations has been studied acoustically previously. However, the mechanism underlying the loss of echogenicity due to cavitation of ELIP has not been fully clarified. In this study, an ultra-high speed imaging approach was employed to observe the destruction phenomena of single ELIP exposed to ultrasound bursts at a center frequency of 6- MHz. We observed a rapid size reduction during the ultrasound excitation in 139 out of 397 (35 %) ultra-high-speed recordings. The shell dilation rate, which is defined as the microbubble wall velocity divided by the instantaneous radius, $\dot{R}/R$, was extracted from the radius versus time response of each ELIP, and was found to be correlated with the deflation. Fragmentation and surface mode vibrations were also observed and are shown to depend on the applied acoustic pressure and initial radius. Results from this study can be utilized to optimize the theranostic application of ELIP, e.g., by tuning the size distribution or the excitation frequency.

Keywords

ultrasound contrast agents; microbubbles; echogenic liposomes; cavitation

1. Introduction

Micron-sized encapsulated bubbles are widely used as blood-pool ultrasound contrast agents (UCAs) for diagnostic imaging. The gas core provides a large impedance mismatch with

Corresponding Author: Jason L. Raymond (jason.lawrence.raymond@gmail.com).

[a]This work was performed while the first author was a visiting fellow at the Department of Biomedical Engineering, Thoraxcenter, Erasmus Medical Center, Rotterdam, Netherlands.

[b]Present address: Dept. of Engineering Science, University of Oxford, Parks Road, Oxford, OX1 3PJ, United Kingdom

tissue and is therefore highly echogenic. The gas core also expands and contracts nonlinearly under the influence of an acoustic pressure wave. Detection of the nonlinear scattered signals can provide further enhancement of contrast in a region containing UCAs, such as in the circulation and highly perfused organs. The stability of UCAs is essential for diagnostic imaging techniques, such as perfusion imaging, where the bubbles provide enhanced contrast for visualizing areas of high blood volume. The microbubble population can also be readily depleted during ultrasound imaging using pulses with peak rarefactional pressures larger than about 1 MPa (Chomas *et al* 2001b). Following a depletion pulse, the assessment of perfusion of new contrast agent microbubbles flowing into the depleted region can assist diagnosis of cardiac ischemia and angiogenic tumors (Cosgrove and Harvey 2009, Wilson and Burns 2010). Novel imaging methods have been emerging which utilize the intentional destruction of UCA microbubbles, such as: disruption-reperfusion imaging, flash echo and stimulated acoustic emission imaging. Ultrasound-mediated UCA destruction has also been shown to be beneficial in certain therapeutic applications, such as localized drug delivery (Schroeder *et al* 2009, Sutton *et al* 2013, Kooiman *et al* 2014) and thrombolysis (Petit *et al* 2015).

Ultrasound-induced UCA destruction resulting from transient acoustic activation of the microbubbles (or cavitation) has been the subject of previous investigations (Sboros 2008, Wrenn *et al* 2012). Both acoustical measurements (Chen *et al* 2003, Porter *et al* 2006, Smith *et al* 2007, Yeh and Su 2008) and high-speed optical observations (Dayton *et al* 1999, Chomas *et al* 2000, Postema *et al* 2005a, 2005b, Lindsey *et al* 2015, Kothapalli *et al* 2015) have been used to detect irreversible destruction of UCAs above a certain acoustic pressure threshold. The threshold varies with the frequency, pulse length and the strength of the encapsulating shell (Chen *et al* 2003, Borden *et al* 2005, Smith *et al* 2007, Radhakrishnan *et al* 2013). Two regimes of ultrasound-induced UCA destruction have been classified based on the temporal dynamics of gas loss: acoustically driven diffusion and rapid fragmentation (Chomas *et al* 2001a, Porter *et al* 2006). At relatively low pressures (MI < 0.2), oscillations of the microbubbles can disrupt the encapsulating shell, resulting in deflation or shrinkage of the microbubble (Chomas *et al* 2001a, Chen *et al* 2002, Borden *et al* 2005, Guidi *et al* 2010) – this mechanism is termed acoustically driven diffusion in order to differentiate it from static diffusion of gas out from an undriven microbubble. At a higher pressure regime (MI > 0.2), the bubble expansion ratio can become so large that the wall acceleration is dominated by the inertia of the surrounding liquid (Leighton 1994), leading to violent collapse of the bubble. During this process the bubble can fragment or break into small pieces forming daughter bubbles and emitting broadband noise (Chomas *et al* 2001b, Chen *et al* 2003).

Special attention has been given to investigating the evolution of UCA response when exposed to ultrasound in order to develop contrast specific imaging methods and drug delivery procedures (Ferrara *et al* 2009, Wrenn *et al* 2012, Kooiman *et al* 2014, de Saint Victor *et al* 2014). Early work using ultrasound pulse-echo techniques suggested an enhancement in backscattering immediately after UCA disruption for acoustic pressures exceeding a threshold, resulting from liberation of the encapsulated gas and generation of a free-air bubble (Bouakaz *et al* 1999, Chen *et al* 2002, Ammi *et al* 2006, Bevan *et al* 2007). The subsequent shrinkage and passage of the bubble through resonant size during deflation was also shown to contribute to an enhanced scattering effect (Chen *et al* 2002). Recently,

acoustically-induced deflation of UCAs exposed to ultrasound and the corresponding change in vibration dynamics of the encapsulated gas microbubble has been investigated optically (Chetty *et al* 2008, Guidi *et al* 2010, Thomas *et al* 2012, Viti *et al* 2012, Lindsey *et al* 2015). Ultra-high-speed imaging studies of UCAs exposed to pulsed ultrasound have revealed microbubble deflation due to individual sub-threshold pulses (Thomas *et al* 2012, Viti *et al* 2012). The amplitude of radial oscillations was indeed observed to increase for microbubbles close to resonance size (van der Meer *et al* 2007, Chetty *et al* 2008, Thomas *et al* 2012).

Investigations of UCA response have been further extended to echogenic liposomes (ELIP), which are a novel agent showing potential for theranostic use (Britton *et al* 2010, Radhakrishnan *et al* 2012). ELIP are phospholipid vesicles that encapsulate both gas and aqueous cores (Huang 2010, Raymond *et al* 2014). Pressure thresholds for acoustically driven diffusion as well as rapid fragmentation of ELIP have been identified by Smith et al (2007). In a later study by Radhakrishnan et al (2013), the loss of echogenicity from ELIP exposed to pulsed Doppler ultrasound was correlated with acoustic emissions in an attempt to understand the destruction process. In both of these previous studies, 6-MHz duplex spectral Doppler waveforms from a standard clinical diagnostic scanner equipped with a peripheral vascular probe (HDI 5000 with L12-5 linear array transducer, Philips Medical Systems, Bothell, WA, USA) were used to investigate cavitation thresholds and loss of echogenicity from ELIP. Radhakrishnan et al (2013) observed ~50 % loss of echogenicity at acoustic pressure amplitudes well below the measured stable or inertial cavitation thresholds, which were found to be ~500 kPa and ~630 kPa, respectively. Rupture of the shell is thought to play a role in liberation of gas from ELIP (Radhakrishnan *et al* 2013); however, the mechanism responsible for loss of echogenicity at pressure levels below the stable or inertial cavitation threshold is unknown.

In this study, we investigated the destruction phenomena of ELIP exposed to pulsed ultrasound excitations at a center frequency of 6 MHz. An ultra-high-speed imaging camera operating at 19×10^6 frames per second was used to measure the radius versus time dynamics of ELIP in response to 5 consecutive tone bursts over a duration of 400 ms. The acoustic pressure amplitudes were below the previously determined *in vitro* pressure threshold for inertial cavitation of ELIP. Several phenomena were observed including rapid fragmentation, surface mode vibrations, and in some cases, a rapid size reduction during the ultrasound excitation.

2. Materials and Methods

2.1. Experimental setup

Freeze-dried ELIP dispersions consisting of EggPC/DPPC/DPPE/DPPG/Cholesterol (27:42:8:8:15, mol %) were prepared as described by Huang (Huang 2010) [1,2-dipalmitoyl-sn-glycero-3-phosphocholine, Egg phosphocholine (Egg PC); 1,2-dipalmitoyl-sn-glycero-3-phosphocholine (DPPC), 1,2-Dipalmitoyl-sn-glycero-3-phosphoethanolamine (DPPE). 1,2-dipalmitoyl-sn-glycero-3-phospho-(1'-rac-glycerol) (DPPG)]. ELIP were prepared at the University of Texas Health Science Center (Houston, Texas, USA) and shipped overnight to Erasmus Medical Center (Rotterdam, the Netherlands) in lyophilized powder form with

refrigerant packs (4 °C). The lyophilized lipid powder was reconstituted using air-saturated, filtered (Type I) water at room temperature, resulting in stock suspensions of ELIP at a lipid concentration of 10 mg/mL. The stock suspension was diluted (~100×) in air-saturated phosphate-buffered saline (PBS) mixed with 0.5 % (wt./vol.) bovine serum albumin (BSA) solution (Sigma Chemical Co., St. Louis, USA). The diluted suspension was injected into an OptiCell® (Nunc/Thermo Scientific, Wiesbaden, Germany) and placed on a microscope optical stage submerged in a 37 °C water bath for imaging under a microscope with a 60× water-immersion objective (BXFM; Olympus, Zoeterwoude, the Netherlands). The total magnification of the system was increased to 120× using a 2× magnification lens inside the microscope. A xenon flash lamp (A-260, Vision Light Tech, Uden, the Netherlands) with a fiber-optic light guide (Schott AG, Mainz, Germany) was used to illuminate the optical region of interest for the ultra-high-speed recordings. A diagram of the optical imaging setup is presented in Figure 1. Recordings of the bubble dynamics consisting of 128 frames were captured at approximately 19×10^6 frames per second using the ultra-high-speed framing camera Brandaris 128 (Chin *et al* 2003, Gelderblom *et al* 2012). In this study, ELIP with initial radii ($R1$) ranging from 0.5–2.5 μm were analyzed. Previous Coulter counter measurements of the particle size distribution for this ELIP formulation indicated a volume-weighted modal radius of approximately 1 μm for a population of ELIP *in vitro* (Raymond *et al* 2014).

2.2. Acoustic excitation pulse

The excitation waveforms and acoustic pressure amplitude range used in this investigation were selected based on previous studies of ELIP cavitation by Smith et al (2007) and Radhakrishnan et al (2013). Acoustic excitation tone bursts similar to the pulsed Doppler waveforms used in previous studies were applied. Each narrowband burst consisted of a 20-cycle sinusoidal wave with a cosine envelope and a fundamental frequency of 6 MHz. The cosine windowing of the transmit pulse was consistent with the spectral Doppler pulse waveforms measured from a clinical ultrasound imaging system (HDI 5000, Philips, Bothell, WA, USA) (Radhakrishnan et al 2013). We selected four acoustic pressure amplitudes (110, 250, 410, and 580 kPa) which were sufficient to generate observable bubble motion in the optical recording but below the inertial cavitation threshold determined previously (Radhakrishnan *et al* 2013). Waveforms were generated using a programmable arbitrary waveform generator (Model 8026, Tabor Electronics Ltd., Tel Hanan, Israel) and amplified using a wideband RF amplifier (0.3–35 MHz; Model A-500, Electronic Navigation Industries, Rochester, NY, USA) before being routed to a focused, broadband PVDF transducer (PA275; Precision Acoustics, Dorchester, United Kingdom). The transducer had a diameter of 23 mm, and focal distance of 25 mm, with a −6 dB frequency bandwidth from 2.0–13.5 MHz and was positioned in the water bath at a 45° angle below the sample. The acoustic focus (0.5 mm full-width at half-maximum pressure) was aligned with the optical region of interest before the experiment. The ultrasound burst was triggered by the camera and the arrival time of the pulse was calibrated using a pulse-echo waveform obtained from a scattering particle positioned in the optical region of interest prior to the experiment. The uncertainty was on the order of 10 ns, determined by the field of view (45.0×26.3 μm) and the speed of sound, which was kept constant throughout the experiment (the temperature of the water bath was controlled at 37 °C).

The acoustic pressure at four driving amplitudes was calibrated using a 0.2-mm PVDF needle-type hydrophone (sensitivity 45 nV/Pa ± 6% uncertainty; Precision Acoustics Ltd., Dorchester, UK). The hydrophone was positioned approximately 2 mm from the membrane of a modified OptiCell® (one of the membranes was removed to allow hydrophone access for calibration) and the peak acoustic pressure *in situ* at the location of the bubble during the optical recordings was determined to be 110, 250, 410, and 580 kPa. The *in situ* acoustic pressure was attenuated by a factor of approximately 3 dB relative to the free-field pressure due to the presence of the OptiCell® membrane and the 45° angle of incidence of the acoustic wave. The measured *in situ* pressure waveform for a 250 kPa peak pressure excitation pulse is shown in Figure 2.

2.3. Data reduction and analysis

The Brandaris 128 ultra-high-speed framing camera is able to store up to 6 sequences of 128 frames in memory, allowing multiple recordings to be acquired in a single run. The timing between recordings is determined by readout of the CCD image sensors, which results in an approximate 80 ms delay between consecutive recordings (Chin *et al* 2003). For each individual ELIP selected for investigation, 6 recordings were acquired sequentially over an interval of 400 ms. The first recording was acquired without ultrasound excitation to determine the quiescent resting radius of the stabilized microbbuble. Ultrasound tone bursts at one of the driving pressure amplitudes (110, 250, 410, or 580 kPa) were applied for each of the 5 subsequent recordings. The bubble radius as a function of time, $R(t)$, was measured from each recording using custom image analysis and tracking software developed in MATLAB (the Mathworks, Natick, MA, USA) (van der Meer *et al* 2007). Time-domain interpolation using the fast Fourier transform was used to recover the signal for analysis due to the low number of samples per cycle (~3) available from the optical recordings. Briefly, the 128-point $R(t)$ signal was transformed to the Fourier domain, zero-padded, and then transformed back with 8× resampling using the MATLAB *interpft* routine (Lyons 2011).

Individual ELIP were exposed to 5 consecutive ultrasound tone bursts at one of the four pressure amplitudes described above. We considered each ultra-high-speed recording of a tone burst excitation an independent trial. A typical radius versus time curve for a single recording is shown in Figure 3a. The initial radius (R_1) and the final radius (R_2) were estimated based on the mean value of the $R(t)$ curve during the 8 frames at the beginning and the end of the recording, respectively.

For the example shown in Figure 3a, we observed a noticeable change in radius ($\Delta R = R_2 - R_1$) as a result of the acoustic excitation. The change was considered significant if the absolute size change of ELIP is greater than a predetermined resolution limit given by $|\Delta R| = |R_2 - R_1| \geq R_L$ (where R_L = 0.12 μm, or approximately 1.33 times the pixel dimension in the images, 90 nm). The resolution limit, R_L, was established using the method described by Emmer et al (2007), briefly, the maximum absolute variation in radius measured during the first recording (128 frames when no ultrasound was applied) was used as an estimate of the stochastic error and the average variation measured for all ELIP was taken as the resolution limit.

For the radius versus time curve presented in Figure 3a, the final radius was smaller than the initial radius ($R_2 < R_1$). Therefore we posit that partial deflation of the ELIP occurred during the 20-cycle burst excitation. During the deflation, the mean radius about which the bubble is oscillating is changing with time which poses a complication in analyzing the oscillation amplitude. Therefore, we consider the time derivative of the radius response which gives the microbubble wall velocity, $\dot{R}$, or dilatation rate, $\dot{R}/R$, in order to analyze of the vibrational response. For monofrequency vibrations the dilatation rate can be approximated as $\dot{R}/R \approx 2\pi f \Delta R/R_0$ (van der Meer *et al* 2007). The wall velocity and dilatation rate were calculated directly from the experimentally measured radius versus time curves and the result is shown in Figure 3b.

3. Results

A total of 397 radius versus time curves for ELIP with initial radii (R_1) ranging from 0.5–2.5 μm were analyzed. Results are presented as follows. In the first two subsections, we describe observed phenomena which stem from instabilities in the volumetric oscillations. In the third subsection, the radius versus time responses of ELIP are analyzed.

3.1. Fragmentation

Fragmentation was indicated by the appearance of several smaller (daughter) bubble fragments in the image frame following collapse of the bubble during the acoustic tone burst excitation. The bubble fragments continued to vibrate under the influence of acoustic excitation, but were observed to disappear quickly and were not visible at the end of the ultra-high-speed recording. Fragmentation was not observed at 110 or 250 kPa peak pressures. Fragmentation of the microbubble into daughter bubbles was observed in 5 of 153 (3 %) recordings at 410 kPa and 6 of 51 (12 %) recordings at 580 kPa peak pressure. Figure 4 shows an example of microbubble fragmentation for a 580 kPa peak pressure tone burst. The initial radius, R_1, is 0.75 μm (shown in frame #11 before the pressure wave arrives). The microbubble is shown compressing in frame #29 and expanding during the negative pressure half-cycle in frames #30 and #31. The compressed microbubble is not visible in frame #32. Upon rebounce three fragments appear in frame #33 which subsequently grow under the influence of the negative acoustic driving pressure. The fragments undergo several more oscillations before dissolving completely in frame #60 (not shown) while the ultrasound tone burst was still on. For this example, the largest radius measured before fragmentation, R_{max}, is 1.5 μm (frame #31) giving a maximum expansion ratio, $R_{max}/R_1 \sim 2$. The initial radius (R_1) and maximum expansion ratio (R_{max}/R_1) for each ELIP observed to fragment is given in Table 1. For all of the ELIP observed to fragment the initial radii were in a narrow range between 0.75–1.05 μm and the maximum expansion ratios were between 1.46 and 2.24.

3.2. Surface modes

Surface mode vibrations were also observed, and we posit that these vibrations manifest as oscillating asymmetric patterns in the images at a vibration frequency lower than the acoustic driving frequency. An impartial observer evaluated the recordings and indicated for each if a surface mode oscillation was observed (yes or no). The appearance of oscillating asymmetric patterns at a frequency lower than the pulsation mode frequency was taken to be

indicative of a surface mode vibration. Such vibrations did not preclude the recording from further analysis of the radius versus time response.

Surface mode vibrations were observed in 147 out of 397 total recordings (37 %). Figure 5 illustrates the response of a 2.2 μm ELIP excited by 6-MHz tone burst with an peak pressure amplitude of 580 kPa. Asymmetric patterns indicative of surface mode oscillations are first visible in frame #32, after several cycles of acoustic excitation. During subsequent acoustic cycles, the surface mode oscillation amplitude grows and aspherical radial perturbations are evident about the perimeter of the microbubble. A summary of the number of recordings in which surface mode vibrations were observed for each peak pressure level is given in Table 2. Observations of surface modes occurred with higher incidence at larger peak acoustic pressures: 15 % at 110 kPa, 30 % at 250 kPa, 51 % at 410 kPa, and 55 % at 580 kPa, over all initial radii. Surface modes were also found to occur more frequently in larger ELIP: 84 % for ELIP with initial radii greater than or equal to 1.5 μm versus 13 % for ELIP with initial radii less than 1.5 μm, at 580 kPa. Examples of surface mode vibrations observed for ELIP with initial radii of 1.8, 2.0 and 2.2 μm are shown in Figure 6.

3.3. Stable volume oscillations

A total of 386 radius versus time curves for 88 individual ELIP were analyzed to evaluate the radial response of ELIP under consecutive pulsed ultrasound excitations. The data set includes recordings of ELIP undergoing stable volumetric oscillations both with (n = 147) and without (n = 239) surface mode vibrations. In all cases, the radius versus time curves representing the volumetric expansion and compression were derived using a minimum cost algorithm to yield the mean radius averaged over at least 90 equally spaced angles (van der Meer *et al* 2007). ELIP that fragmented were not included in the analysis.

A typical radius versus time sequence consisting of 6 recordings for an individual ELIP is shown in Figure 7a. In this run, we observed deflation from an initial resting radius of 1.33 μm to a final resting radius of 0.49 μm following 5 consecutive ultrasound bursts at 110 kPa peak acoustic pressure. For each tone burst excitation, deflation of up to 20 % change in radius occurs during the 3.33 μs acoustic excitation, while no observable change in radius occurs during the relatively long acoustic quiescent time period (~80 ms) between recordings. The deflation process takes place in stages corresponding to periods when the microbubble is acoustically driven by a tone bust excitation. As illustrated in Figure 7a, both the radial oscillation amplitude and the time-dependent dilatation rate vary from burst to burst. The dilatation rate ($\dot{R}/R$) and change in resting radius before and after the excitation ($|\Delta R|$) are maximum during recording #3 (the second ultrasound tone burst excitation) as the ELIP deflates and goes through an apparent resonance size. The maximum dilatation rate was 2.3×10^{7} s^{-1} and the initial quiescent radius of the microbubble was 1.10 μm during this recording. The maximum dilatation rate decreases with each subsequent excitation and nearly complete deflation (95 % reduction in volume) is observed after 5 consecutive ultrasound tone burst excitations. In Figure 7b, plots of the absolute change in radius and the maximum dilatation rate derived from each of the recordings are overlaid, which illustrates that these metrics are closely correlated.

Figure 8 shows the resultant change in radius, ΔR, as a function of the initial size due to single ultrasound tone burst excitations at 110, 250, 410 and 580 kPa, respectively. The filled data points indicate recordings in which surface mode vibrations were observed. A total of 139 (35 %) ELIP showed significant deflation (defined as $\Delta R = R_2 - R_1 < -R_L$) during a single burst excitation. The maximum relative change in radius was −21 %, −29 %, −46 % and −43 % for 110, 250, 410 and 580 kPa excitations, respectively. Additionally, at each pressure, the maximum size reduction is dependent on the size and generally occurs for smaller ELIP near the apparent resonance size (1 μm).

Figure 9 shows the resultant change in radius as a function of the maximum dilatation rate. Two regimes can be observed. At low dilatation rates ($< 3.4\times10^6$ s^{-1}) no significant size change is observable; the maximum size variation is comparable to the resolution limit or uncertainty in the optical measurement ($|\Delta R| < R_L$). At higher dilatation rates ($> 3.4\times10^6$ s^{-1}) all of the measured bubbles deflate to a certain degree ($\Delta R < 0$). A change point analysis technique based on segmented linear regression using the mean square error (MSE) estimator was used to detect the transition point between the first regime, in which the mean variation was constrained to zero, and second regime, in which the mean variation was non-zero and therefore a change of size was evident as a function the dilatation rate (Qiu 2005). The change point at a dilatation rate of 3.4×10^6 s^{-1} demarcates the threshold for the occurrence of ELIP deflation.

4. Discussion

4.1. Fragmentation

Fragmentation of a phospholipid encapsulated bubble into smaller bubbles at high acoustic pressure amplitudes (Table 1) is a common phenomenon that has been described in detail previously (Chomas *et al* 2000, Lindsey *et al* 2015, Dayton *et al* 1999). One likely mechanism is that surface instabilities generated during the inertially driven collapse lead to fragmentation during the subsequent growth phase (Chomas *et al* 2001a, Leighton 1994). The inertially driven collapse also promotes broadband acoustic emissions, which have been used extensively to characterize the threshold for fragmentation of ELIP (Radhakrishnan *et al* 2013) as well as other UCAs (Chen *et al* 2003, King *et al* 2010, Lindsey *et al* 2015). In preliminary experiments, we frequently observed breakup of ELIP microbubbles into smaller fragments when they were exposed to pressure amplitudes higher than those ultimately used in this study (> 580 kPa). As we aim at studying the loss of echogenicity due to stable cavitation, and for the simplicity of radius versus time analysis, the maximum pressure selected for this study was 580 kPa. This value was approximately 10 % below the threshold for inertial cavitation at 6 MHz measured previously for a population of ELIP (Radhakrishnan *et al* 2013). The low occurrence of fragmentation in this study is therefore attributed to the use of excitation pressures that are lower than the previously measured threshold. Fragmentation was observed despite operating below the inertial cavitation threshold, although only for a narrow size range (0.75–1.05 μm, Table 1) and only at the two highest pressure levels used in this study (410 kPa and 580 kPa, Table 1). This can be attributed to ELIP which are optimally sized, and therefore more likely to undergo inertial collapse due to the applied ultrasound pulse at 6-MHz fundamental frequency. Gas nuclei

which are optimally sized at a particular excitation frequency tend to undergo inertial cavitation at lower threshold pressures (Apfel and Holland 1991). The size range of ELIP observed to fragment in this study corresponded to the expected resonance size for ELIP at 6 MHz (see Fig. 5 in Raymond et al 2015). ELIP suspensions are known to contain particles as small as tens of nanometers (Kopechek *et al* 2011). However, Coulter counter measurements of the size distribution indicate a volume-weighted modal radius of approximately 1 μm for the ELIP formulation used in this study (see Figure 2d in Raymond *et al* 2014). Therefore, a large proportion of ELIP particles within a population have radii within the range most likely to fragment above a pressure threshold using 6-MHz ultrasound tone bursts.

4.2. Surface modes

Oscillating patterns indicative of surface mode vibrations were observed in 37 % of the recordings. Surface mode instabilities are known to be threshold dependent and readily excitable for bubbles larger than volumetric resonance (Neppiras 1980, Leighton 1994). Moreover, because surface modes are strongly coupled to the volumetric pulsation mode, they are normally excited after several acoustic cycles and at lower frequencies than the pulsation mode (Brenner *et al* 1995, Dollet *et al* 2008, Versluis *et al* 2010). Surface modes occurred predominately for ELIP with initial radii greater than 1.5 μm. Surface mode vibrations were not observed to result in fragmentation or splitting of ELIP in this study.

4.3. ELIP deflation and possible mechanisms

The observations of ELIP undergoing stable volumetric oscillations indicates that the deflation process occurs in stages and predominately during the ultrasound exposure (Figure 7). This is in agreement with previously reported phenomena for other lipid-shelled UCAs (Chomas *et al* 2001a, Thomas *et al* 2012, Viti *et al* 2012). The most significant difference between commercially available lipid-shelled UCAs and the ELIP formulation used in this study is the gas content. The ELIP used in this study contained air, which is more soluble in aqueous solution than high molecular weight gases used in second-generation commercial UCAs. Furthermore, commercially available UCAs are typically encapsulated by a lipid monolayer shell which has limited capability to load with drugs. ELIP are bilayer liposomes that can carry both gas and drugs in a single particle. This is important since it makes ELIP both a contrast agent as well as a drug carrier which can be responsive to ultrasound for content release. Despite these differences, it has been shown in previous studies that ELIP behave similarly to other UCAs (Raymond *et al* 2014, Raymond *et al* 2015). We are the first group to show that such novel agents can be used for both image enhancement as well as therapeutic delivery, including the release of bioactive gases (Britton *et al* 2010, Kim *et al* 2014, Sutton *et al* 2014).

It is important to note that broadband impulse excitations (pulse duration of 0.33 μs, 1.5 cycles at 4 MHz center frequency) up to 500 kPa peak pressure did not result in enhanced gas diffusion in a previous study (Raymond *et al* 2015). However, in this study narrowband 20-cycle Doppler tone burst excitations resulted in enhanced gas diffusion at peak acoustic pressures as low as 110 kPa. Figure 8 illustrates that 35 % of ELIP underwent a detectable size reduction ($\Delta R < 0.12$ μm) after exposure to a single 6-MHz ultrasound tone burst.

One of the possible physical processes involved in the deflation phenomenon is acoustically driven diffusion, which is an increased convective diffusion process driven by the ultrasound exposure. This phenomenon has been observed previously for ELIP (Smith *et al* 2007) as well as other UCAs (Chomas *et al* 2001a, Porter *et al* 2006). Lipid shell destruction can occur simultaneously - whereby ultrasound-assisted budding, buckling, and other mechanisms can cause disruption of the lipid shell resulting in lipid shedding (O'Brien *et al* 2013), or the expulsion of sub-micron fragments which cannot be resolved optically (Borden *et al* 2005). Recent studies based on high-speed fluorescence imaging of microbubbles exposed to burst excitations have revealed the detachment of lipid particles within a few acoustic cycles and the subsequent transport process of the particles by the surrounding streaming flow field (Gelderblom *et al* 2013, Luan *et al* 2014). Cox and Thomas (2013) have suggested that these particles must entrain a finite volume of gas in order for accelerated dissolution to occur. In this way, sub-micron fragments are pinched off leading to a corresponding reduction in size of ELIP, which may be associated with lipid shedding and trigger the process of acoustically driven diffusion. Gas loss from phospholipid-shelled microbubbles results in a decrease in the encapsulated gas volume, and concomitant reduction in the surface area of the shell. Therefore, less surfactant material is required to stabilize the deflated gas core and excess lipids are expelled during deflation.

Smith et al. (2007) and Radhakrishnan et al. (2013) previously investigated ELIP destruction thresholds using 6.0-MHz Doppler pulses with the same pulse duration used in this study (3.33 μs). Smith et al. (2007) found the threshold for acoustically driven diffusion occurs at a peak rarefactional pressure of 480 kPa, which corresponds to the threshold for stable cavitation emissions found by Radhakrishnan et al. (2013). In this optical study, 51 % of individual ELIP deflated at 410 kPa and 55 % at 580 kPa, compared to only 14 % at 110 kPa and 30 % at 250 kPa. The onset of acoustically driven diffusion based on observations of single ELIP in this study is in general agreement with previous acoustic investigations which identified a threshold for this effect on a population of ELIP.

The observations suggest an accelerated deflation for ELIP with initial radii near an apparent resonance radius of ~1 μm, where radial (volumetric) oscillation amplitudes are largest (Figure 8). For the size range of ELIP considered in this study (and in general, for microbubbles with radii less than about 3 μm) the dynamic response is dominated by the viscoelastic properties of the surrounding fluid with an additional contribution to damping from the shell dilatation viscosity. Therefore, the dynamics can depend not only on the size and shell properties, but also on the properties of the surrounding medium and the insonation frequency (Helfield *et al* 2016b, 2016a). We did not explore frequency as an independent parameter in this study. However, the experimental data indicated a strong dependence of ELIP deflation on the dilatation rate (Figure 9). Similar correlations have been reported for UCA microbubbles using both optical and acoustical techniques (Guidi *et al* 2010, Thomas *et al* 2012).

4.4. Evolution of acoustic responses during deflation

Ultra-high-speed imaging is a direct method to characterize the evolution of ELIP acoustic responses under consecutive ultrasound tone bursts. The results of this study suggest that the

oscillation dynamics of ELIP undergo irreversible changes during deflation (Figure 7). Our observations are consistent with previous studies based on both acoustical and optical methods which have shown that lipid shelled microbubbles may undergo irreversible deflation in response to ultrasound-induced oscillations, and that the response of deflating bubbles may change over subsequent pulses depending on their instantaneous radius (Couture *et al* 2009, Guidi *et al* 2010, Thomas *et al* 2012). Depending on the acoustic pressure, ELIP with initial radii near or slightly larger than resonance may deflate during excitation by an ultrasound tone burst. During subsequent tone bursts, the amplitude of oscillation will increase as the bubble further deflates through the resonance size. Therefore, ultrasound tone bursts at pressure amplitudes below the threshold for rapid fragmentation can potentially be used to promote acoustically driven diffusion and to affect the controlled deflation of ELIP.

4.5. Clinical implications

Results of this study can be used to improve strategies for ultrasound-controlled gas delivery to vascular tissue beds using ELIP (Britton *et al* 2010, Kim *et al* 2014, Sutton *et al* 2014, Fix *et al* 2015). Results suggest that two parameters should be carefully considered in order to trigger enhanced diffusion of an encapsulated gas under pulsed ultrasound excitation. First, the acoustic pressure should be sufficient to drive the dilatation rate above a certain threshold, 3.4×10^{6} s^{-1} in this study at 6 MHz (Figure 9) to initiate the fast deflation of ELIP. According to the observations from this study, if inertial cavitation (fragmentation) is to be avoided, a peak pressure amplitude of 250 kPa is a reasonable choice at 6 MHz. Second, the size distribution of ELIP may influence the duration and temporal release profile of the encapsulated gas. ELIP near resonance size will generate a larger instantaneous response to acoustic excitation, which will likely decay over time as the bubbles deflate in response to acoustic excitation. However, a higher proportion of larger ELIP (> 2 μm in radius) within a population may be preferable for theranostic use because they scatter ultrasound effectively in the diagnostic frequency range (Raymond *et al* 2014) and are less likely to undergo acoustically driven diffusion or rapid fragmentation due to individual sub-threshold ultrasound tone bursts. ELIP initially larger than resonance may achieve maximum therapeutic efficacy at a later stage when passing through the resonance size due to static dissolution in the circulation (Kabalnov *et al* 1998). Moreover, larger ELIP can be used to deliver a much higher volume of gas as payload compared to smaller bubbles.

For controlled delivery of encapsulated gas via ELIP, stable cavitation accompanied by the acoustically driven diffusion mechanism (Figure 7) may be preferable to rapid fragmentation (Figure 4) to avoid negative bioeffects associated with inertial cavitation. The observed phenomena could be exploited to optimize the theranostic application of ELIP, either by adjusting the size distribution of ELIP within a population or the excitation frequency. It has recently been demonstrated that monodisperse drug-loaded ELIP in a clinically relevant size range can be manufactured using microfluidic devices (Kandadai *et al* 2016). Microfluidic sorting techniques (Segers and Versluis 2014, Kok *et al* 2015) can also be used to obtain a monodisperse bubble population of a particular size. These technologies may allow the size distribution of ELIP to be tailored for specific ultrasound frequencies. To first-order approximation the dilatation rate scales directly with the driving frequency and amplitude of

radial oscillations and is maximum for bubbles near resonance. Operating at a frequency below resonance implies that larger amplitude oscillations would need to be obtained in order to promote acoustically driven diffusion. In this regime, rapid fragmentation may play a more significant role thus imposing a limitation on the lowest frequency suitable to promote acoustically driven diffusion if inertial cavitation is to be avoided.

4.6. Limitations

Limitations of the optical system resolution can result in a bias of the size range of ELIP selected for analysis. The smallest individual ELIP that was measured in this study (0.5 μm) was close to the resolution limit of the ultra-high-speed imaging system (0.4 μm; Chin et al 2003) and ELIP smaller than this limit could not be investigated.

Another limitation is the frame rate of the ultra-high-speed imaging system (19×10^6 frames per second), which only permitted ~3 samples per acoustic cycle. Ultraharmonics and nonlinear oscillations with frequency content higher than about 9.5 MHz were not resolved. It is also likely that minimum or maximum excursions would not be captured in any particular frame given the low number of frames captured per cycle. Therefore, the expansion ratios given in Table 1 should be considered approximations (lower bounds) of the true values.

Two additional factors regarding detection of ELIP deflation using the optical system should be considered. First, the presence of a rigid OptiCell® membrane may contribute to nonspherical oscillations of ELIP and expulsion of fragments in the orthogonal plane which could not be observed optically in this study but have been observed previously (Vos *et al* 2008, Luan *et al* 2014). The OptiCell® may also influence the amplitude of surface mode vibrations. Dollet *et al* (2008) used optical trapping to manipulate the bubble position and found that bubbles nearby the Opticell® wall deform much less in the imaging plane than free-floating bubbles. Second is the generation and ejection of sub-micron fragments which could not be resolved optically (Borden *et al* 2005). Fluorescence studies (Gelderblom *et al* 2013, Luan *et al* 2014) have revealed that this lipid-shedding phenomenon plays an important role in deflation of lipid-shelled UCA. The shedding of sub-micron fragments that entrap gas has been proposed as a possible mechanism to explain the observed rapid deflation of lipid-shelled microbubbles in response to acoustic excitation (Cox and Thomas 2013).

5. Conclusions

In this study, ultra-high-speed optical imaging was used to investigate the acoustic responses of ELIP exposed to 20-cycle Doppler tone bursts. The results suggest that ELIP dynamics in response to pulsed acoustic forcing at 6 MHz are strongly dependent on the instantaneous radius. A peak pressure in excess of approximately 250 kPa is necessary to initiate the fast deflation of ELIP. In general, ELIP are more rapidly deflated at resonance, where the wall velocity is the highest.

Acknowledgments

The authors would like to thank Robert Beurskens and Frits Mastik from the Dept. of Biomedical Engineering, Erasmus Medical Center for technical assistance with Brandaris experiments and Abby Bull (University of Cincinnati) for assistance evaluating the recordings. T.D. Mast (University of Cincinnati) offered helpful comments regarding the signal processing. JLR was supported by a fellowship from the Whitaker International Program administered by the Institute of International Education (IIE). This work was supported in part by the U.S. Department of Health and Human Services, National Institutes of Health (NIH R01HL74002, NIH R01HL059586) and NanoNextNL, a micro and nanotechnology consortium of the Government of the Netherlands and 130 partners.

References

Ammi AY, Cleveland RO, Mamou J, Wang GI, Bridal SL, O'Brien WD Jr. Ultrasonic contrast agent shell rupture detected by inertial cavitation and rebound signals. IEEE Trans Ultrason Ferroelectr Freq Control. 2006; 53:126–135. [PubMed: 16471439]

Apfel RE, Holland CK. Gauging the likelihood of cavitation from short-pulse, low-duty cycle diagnostic ultrasound. Ultrasound Med.Biol. 1991; 17:179–185. [PubMed: 2053214]

Bevan PD, Karshafian R, Tickner EG, Burns PN. Quantitative Measurement of Ultrasound Disruption of Polymer-Shelled Microbubbles. Ultrasound in Medicine and Biology. 2007; 33:1777–1786. [PubMed: 17656011]

Borden MA, Kruse DE, Caskey CF, Zhao S, Dayton PA, Ferrara KW. Influence of lipid shell physicochemical properties on ultrasound-induced microbubble destruction. IEEE Trans Ultrason Ferroelectr Freq Control. 2005; 52:1992–2002. [PubMed: 16422411]

Bouakaz A, Frinking PJ, de Jong N, Bom N. Noninvasive measurement of the hydrostatic pressure in a fluid-filled cavity based on the disappearance time of micrometer-sized free gas bubbles. Ultrasound Med.Biol. 1999; 25:1407–1415. [PubMed: 10626628]

Brenner MP, Lohse D, Dupont TF. Bubble shape oscillations and the onset of sonoluminescence. Physical Review Letters. 1995; 75:954–957. [PubMed: 10060160]

Britton GL, Kim H, Kee PH, Aronowski J, Holland CK, McPherson DD, Huang SL. In vivo therapeutic gas delivery for neuroprotection with echogenic liposomes. Circulation. 2010; 122:1578–1587. [PubMed: 20921443]

Chen W-S, Matula TJ, Brayman AA, Crum LA. A comparison of the fragmentation thresholds and inertial cavitation doses of different ultrasound contrast agents. J.Acoust.Soc.Am. 2003; 113:643–651. [PubMed: 12558300]

Chen W-S, Matula TJ, Crum LA. The disappearance of ultrasound contrast bubbles: Observations of bubble dissolution and cavitation nucleation. Ultrasound Med.Biol. 2002; 28:793–803. [PubMed: 12113792]

Chetty K, Stride E, Sennoga C, Hajnal J, Eckersley R. High-speed optical observations and simulation results of SonoVue microbubbles at low-pressure insonation. IEEE Trans. Ultrason. Ferroelectr. Freq. Control. 2008; 55:1333–1342. [PubMed: 18599421]

Chin CT, Lancée C, Borsboom J, Mastik F, Frijlink ME, De Jong N, Versluis M, Lohse D. Brandaris 128: A digital 25 million frames per second camera with 128 highly sensitive frames. Rev. Sci. Instrum. 2003; 74:5026–5034.

Chomas JE, Dayton PA, May D, Allen J, Klibanov A, Ferrara K. Optical observation of contrast agent destruction. Appl. Phys. Lett. 2000; 77:1056–1058.

Chomas JE, Dayton P, Alien J, Morgan K, Ferrara KW. Mechanisms of contrast agent destruction. IEEE Trans Ultrason Ferroelectr Freq Control. 2001a; 48:232–248. [PubMed: 11367791]

Chomas JE, Dayton P, May D, Ferrara K. Threshold of fragmentation for ultrasonic contrast agents. J Biomed Opt. 2001b; 6:141–150. [PubMed: 11375723]

Cosgrove D, Harvey C. Clinical uses of microbubbles in diagnosis and treatment. Med. Biol. Eng. Comput. 2009; 47:813–826. [PubMed: 19205774]

Couture O, Bannouf S, Montaldo G, Aubry J-F, Fink M, Tanter M. Ultrafast Imaging of Ultrasound Contrast Agents. Ultrasound in Medicine and Biology. 2009; 35:1908–1916. [PubMed: 19699026]

Cox DJ, Thomas JL. Rapid Shrinkage of Lipid-Coated Bubbles in Pulsed Ultrasound. Ultrasound Med. Biol. 2013; 39:466–474. [PubMed: 23245826]

Dayton PA, Morgan KE, Klibanov AL, Brandenburger GH, Ferrara KW. Optical and acoustical observations of the effects of ultrasound on contrast agents. IEEE Trans. Ultrason. Ferroelectr. Freq. Control. 1999; 46:220–232. [PubMed: 18238417]

Dollet B, van der Meer SM, Garbin V, de Jong N, Lohse D, Versluis M. Nonspherical oscillations of ultrasound contrast agent microbubbles. Ultrasound Med.Biol. 2008; 34:1465–1473. [PubMed: 18450362]

Emmer M, van Wamel A, Goertz DE, de Jong N. The onset of microbubble vibration. Ultrasound Med.Biol. 2007; 33:941–949. [PubMed: 17451868]

Ferrara KW, Borden MA, Zhang H. Lipid-shelled vehicles: engineering for ultrasound molecular imaging and drug delivery. Acc.Chem.Res. 2009; 42:881–892. [PubMed: 19552457]

Fix SM, Borden MA, Dayton PA. Therapeutic gas delivery via microbubbles and liposomes. J. Control. Release. 2015; 209:139–149. [PubMed: 25913365]

Gelderblom EC, Vos HJ, Mastik F, Faez T, Luan Y, Kokhuis TJA, Van Der Steen AFW, Lohse D, De Jong N, Versluis M. Brandaris 128 ultra-high-speed imaging facility: 10 years of operation, updates, and enhanced features. Rev. Sci. Instrum. 2012; 83:103706. [PubMed: 23126773]

Gelderblom, E., Wolbers, F., De Jong, N., Van Den Berg, A., Versluis, M. Time-resolved high-speed fluorescence imaging of bubble-induced sonoporation; Proceedings of Meetings on Acoustics 21st International Congress on Acoustics, ICA 2013 - 165th Meeting of the Acoustical Society of America vol 19 Online; 2013. http://www.scopus.com/inward/record.url?eid=2-s2.0-84878983024&partnerID=40&md5=0775e1e6376d4d12040990b49a29e0ad

Guidi F, Vos HJ, Mori R, de Jong N, Tortoli P. Microbubble characterization through acoustically induced deflation. IEEE Trans.Ultrason.Ferroelectr.Freq.Control. 2010; 57:193–202. [PubMed: 20040446]

Helfield B, Black JJ, Qin B, Pacella J, Chen X, Villanueva FS. Fluid Viscosity Affects the Fragmentation and Inertial Cavitation Threshold of Lipid-Encapsulated Microbubbles. Ultrasound in Medicine and Biology. 2016a; 42:782–794. [PubMed: 26674676]

Helfield B, Chen X, Qin B, Villanueva FS. Individual lipid encapsulated microbubble radial oscillations: Effects of fluid viscosity. J. Acoust. Soc. Am. 2016b; 139:204–214. [PubMed: 26827018]

Huang, S-L. Ultrasound-responsive liposomes *Liposomes: methods and protocols*. In: Weissig, V., editor. Methods in Molecular Biology. Vol. 605. New York, NY: Humana Press; 2010. p. 113-128.

Kabalnov A, Bradley J, Flaim S, Klein D, Pelura T, Peters B, Otto S, Reynolds J, Schutt E, Weers J. Dissolution of multicomponent microbubbles in the bloodstream: 2. Experiment. Ultrasound Med. Biol. 1998; 24:751–760. [PubMed: 9695278]

Kandadai MA, Mukherjee P, Shekhar H, Shaw GJ, Papautsky I, Holland CK. Microfluidic manufacture of rt-PA -loaded echogenic liposomes. Biomed. Microdevices. 2016; 18 Online: https://www.scopus.com/inward/record.uri?eid=2-s2.0-84971254231&partnerID=40&md5=d8ef3510b7c4ca6fe2b463590d225f09.

Kim H, Britton GL, Peng T, Holland CK, McPherson DD, Huang S-L. Nitric oxide-loaded echogenic liposomes for treatment of vasospasm following subarachnoid hemorrhage. Int. J. Nanomed. 2014; 9:155–165.

King DA, Malloy MJ, Roberts AC, Haak A, Yoder CC, O'Brien WD Jr. Determination of postexcitation thresholds for single ultrasound contrast agent microbubbles using double passive cavitation detection. J.Acoust.Soc.Am. 2010; 127:3449–3455. [PubMed: 20550244]

Kok MP, Segers T, Versluis M. Bubble sorting in pinched microchannels for ultrasound contrast agent enrichment. Lab Chip Miniaturisation Chem. Biol. 2015; 15:3716–3722.

Kooiman K, Vos HJ, Versluis M, De Jong N. Acoustic behavior of microbubbles and implications for drug delivery. Advanced Drug Delivery Reviews. 2014; 72:28–48. [PubMed: 24667643]

Kopechek JA, Haworth KJ, Raymond JL, Douglas Mast T, Perrin SR Jr, Klegerman ME, Huang S, Porter TM, McPherson DD, Holland CK. Acoustic characterization of echogenic liposomes: Frequency-dependent attenuation and backscatter. J. Acoust. Soc. Am. 2011; 130:3472–3481. [PubMed: 22088022]

Kothapalli SVV, Daeichin VN, Mastik F, Brodin LÅ, Janerot-Sjoberg B, Paradossi G, De Jong N, Grishenkov D. Unique pumping-out fracturing mechanism of a polymer-shelled contrast agent: An

acoustic characterization and optical visualization. IEEE Trans Ultrason Ferroelectr Freq Control. 2015; 62:451–462. [PubMed: 25768814]

Leighton, TG. The Acoustic Bubble. London: Academic Press; 1994.

Lindsey, BD., Rojas, JD., Dayton, PA. On the Relationship Between Microbubble Fragmentation, Deflation and Broadband Superharmonic Signal Production. 2015.

Luan Y, Lajoinie G, Gelderblom E, Skachkov I, van der Steen AFW, Vos HJ, Versluis M, De Jong N. Lipid shedding from single oscillating microbubbles. Ultrasound Med. Biol. 2014; 40:1834–1846. [PubMed: 24798388]

Lyons, RG. Understanding digital signal processing. Upper Saddle River, NJ: Prentice Hall; 2011.

van der Meer SM, Dollet B, Voormolen MM, Chin CT, Bouakaz A, de Jong N, Versluis M, Lohse D. Microbubble spectroscopy of ultrasound contrast agents. J. Acoust. Soc. Am. 2007; 121:648–656. [PubMed: 17297818]

Neppiras EA. Acoustic cavitation. Phys. Rep. 1980; 61:159–251.

O'Brien J-P, Stride E, Ovenden N. Surfactant shedding and gas diffusion during pulsed ultrasound through a microbubble contrast agent suspension. J. Acoust. Soc. Am. 2013; 134:1416–1427. [PubMed: 23927137]

Petit B, Bohren Y, Gaud E, Bussat P, Arditi M, Yan F, Tranquart F, Allémann E. Sonothrombolysis: The Contribution of Stable and Inertial Cavitation to Clot Lysis. Ultrasound Med. Biol. 2015; 41:1402–1410. [PubMed: 25601463]

Porter TM, Smith DA, Holland CK. Acoustic techniques for assessing the Optison destruction threshold. J.Ultrasound Med. 2006; 25:1519–1529. [PubMed: 17121946]

Postema M, Bouakaz A, Versluis M, de Jong N. Ultrasound-induced gas release from contrast agent microbubbles. IEEE Trans.Ultrason.Ferroelectr.Freq.Control. 2005a; 52:1035–1041. [PubMed: 16118985]

Postema M, van Wamel A, ten Cate FJ, de Jong N. High-speed photography during ultrasound illustrates potential therapeutic applications of microbubbles. Med.Phys. 2005b; 32:3707–3711. [PubMed: 16475770]

Qiu, P. Image processing and jump regression analysis. Hoboken, N.J: John Wiley; 2005.

Radhakrishnan K, Bader KB, Haworth KJ, Kopechek JA, Raymond JL, Huang S-L, McPherson DD, Holland CK. Relationship between cavitation and loss of echogenicity from ultrasound contrast agents. Phys. Med. Biol. 2013; 58:6541–6563. [PubMed: 24002637]

Radhakrishnan K, Haworth KJ, Huang S-L, Klegerman ME, McPherson DD, Holland CK. Stability of Echogenic Liposomes as a Blood Pool Ultrasound Contrast Agent in a Physiologic Flow Phantom. Ultrasound Med.Biol. 2012; 38:1970–1981. [PubMed: 22929652]

Raymond JL, Haworth KJ, Bader KB, Radhakrishnan K, Griffin JK, Huang S-L, McPherson DD, Holland CK. Broadband attenuation measurements of phospholipid-shelled ultrasound contrast agents. Ultrasound Med. Biol. 2014; 40:410–421. [PubMed: 24262056]

Raymond JL, Luan Y, Van Rooij T, Kooiman K, Huang S-L, McPherson DD, Versluis M, De Jong N, Holland CK. Impulse response method for characterization of echogenic liposomes. J. Acoust. Soc. Am. 2015; 137:1693–1703. [PubMed: 25920822]

de Saint Victor M, Crake C, Coussios C-C, Stride E. Properties, characteristics and applications of microbubbles for sonothrombolysis. Expert Opinion on Drug Delivery. 2014; 11:187–209. [PubMed: 24400730]

Sboros V. Response of contrast agents to ultrasound. Adv.Drug Deliv.Rev. 2008; 60:1117–1136. [PubMed: 18486270]

Schroeder A, Kost J, Barenholz Y. Ultrasound, liposomes, and drug delivery: principles for using ultrasound to control the release of drugs from liposomes. Chemistry and Physics of Lipids. 2009; 162:1–16. [PubMed: 19703435]

Segers T, Versluis M. Acoustic bubble sorting for ultrasound contrast agent enrichment. Lab Chip Miniaturisation Chem. Biol. 2014; 14:1705–1714.

Smith DA, Porter TM, Martinez J, Huang S, MacDonald RC, McPherson DD, Holland CK. Destruction thresholds of echogenic liposomes with clinical diagnostic ultrasound. Ultrasound Med.Biol. 2007; 33:797–809. [PubMed: 17412486]

Sutton JT, Haworth KJ, Pyne-Geithman G, Holland CK. Ultrasound-mediated drug delivery for cardiovascular disease. Expert Opin.Drug Deliv. 2013; 10:573–592. [PubMed: 23448121]

Sutton JT, Raymond JL, Verleye MC, Pyne-Geithman GJ, Holland CK. Pulsed ultrasound enhances the delivery of nitric oxide from bubble liposomes to ex vivo porcine carotid tissue. Int. J. Nanomed. 2014; 9:4671–4683.

Thomas DH, Butler M, Anderson T, Emmer M, Vos H, Borden M, Stride E, De Jong N, Sboros V. The quasi-stable lipid shelled microbubble in response to consecutive ultrasound pulses. Appl. Phys. Lett. 2012; 101:71601.

Versluis M, Goertz DE, Palanchon P, Heitman IL, van der Meer SM, Dollet B, de Jong N, Lohse D. Microbubble shape oscillations excited through ultrasonic parametric driving. Phys.Rev.E.Stat.Nonlin Soft Matter Phys. 2010; 82:26321.

Viti J, Mori R, Guidi F, Versluis M, Jong N, Tortoli P. Nonlinear oscillations of deflating bubbles. IEEE Trans. Ultrason. Ferroelectr. Freq. Control. 2012; 59:2818–2824. [PubMed: 23221232]

Vos HJ, Dollet B, Bosch JG, Versluis M, de Jong N. Nonspherical vibrations of microbubbles in contact with a wall: a pilot study at low mechanical index. Ultrasound Med.Biol. 2008; 34:685–688. [PubMed: 18077080]

Wilson SR, Burns PN. Microbubble-enhanced US in body imaging: What role? Radiology. 2010; 257:24–39. [PubMed: 20851938]

Wrenn SP, Dicker SM, Small EF, Dan NR, Mleczko M, Schmitz G, Lewin PA. Bursting bubbles and bilayers. Theranostics. 2012; 2:1140–1159. [PubMed: 23382772]

Yeh C-K, Su S-Y. Effects of Acoustic Insonation Parameters on Ultrasound Contrast Agent Destruction. Ultrasound Med. Biol. 2008; 34:1281–1291. [PubMed: 18343019]

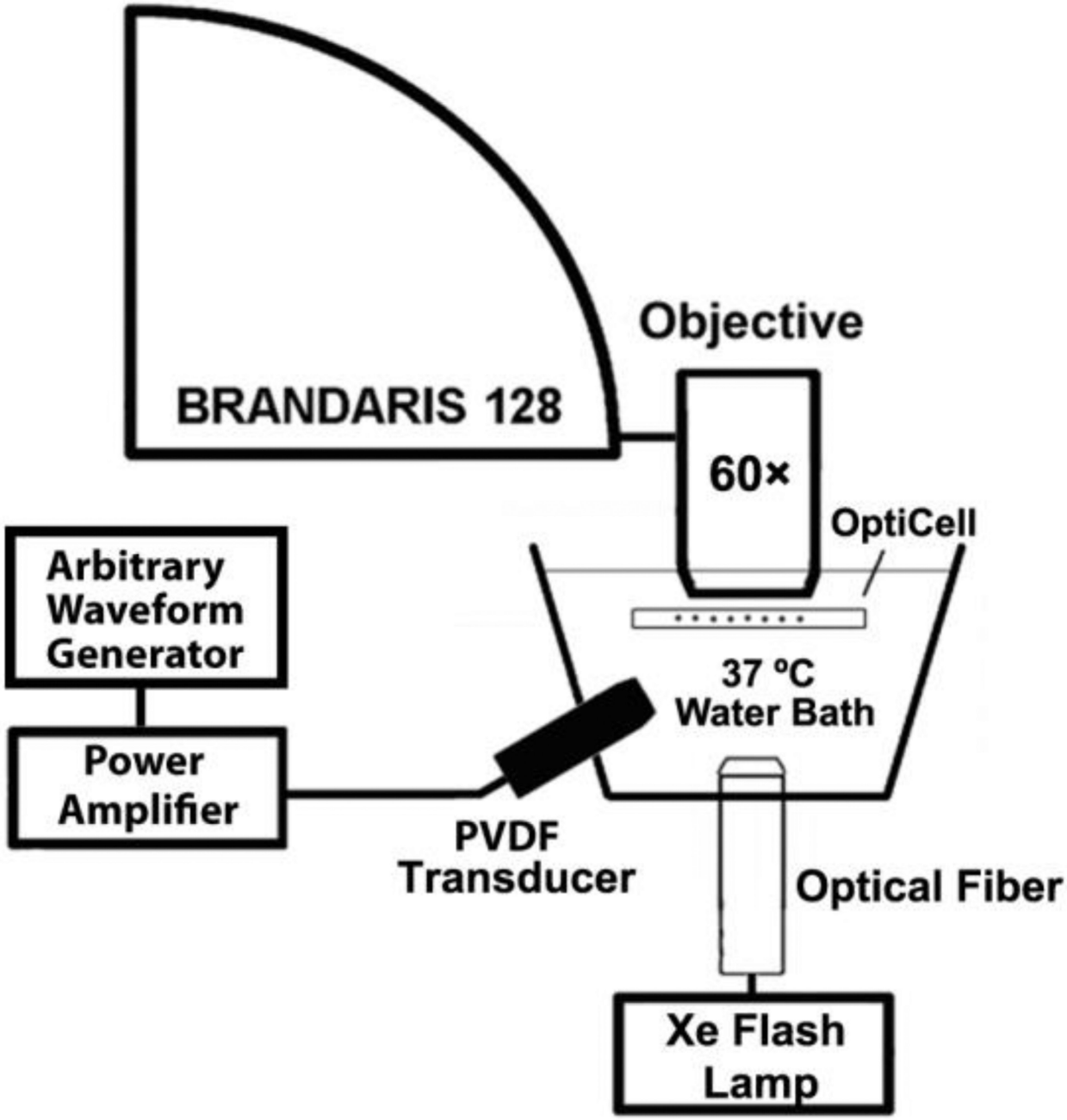

Figure 1.
Schematic of the setup used to optically record the vibration dynamics of echogenic liposomes exposed to pulsed ultrasound excitations.

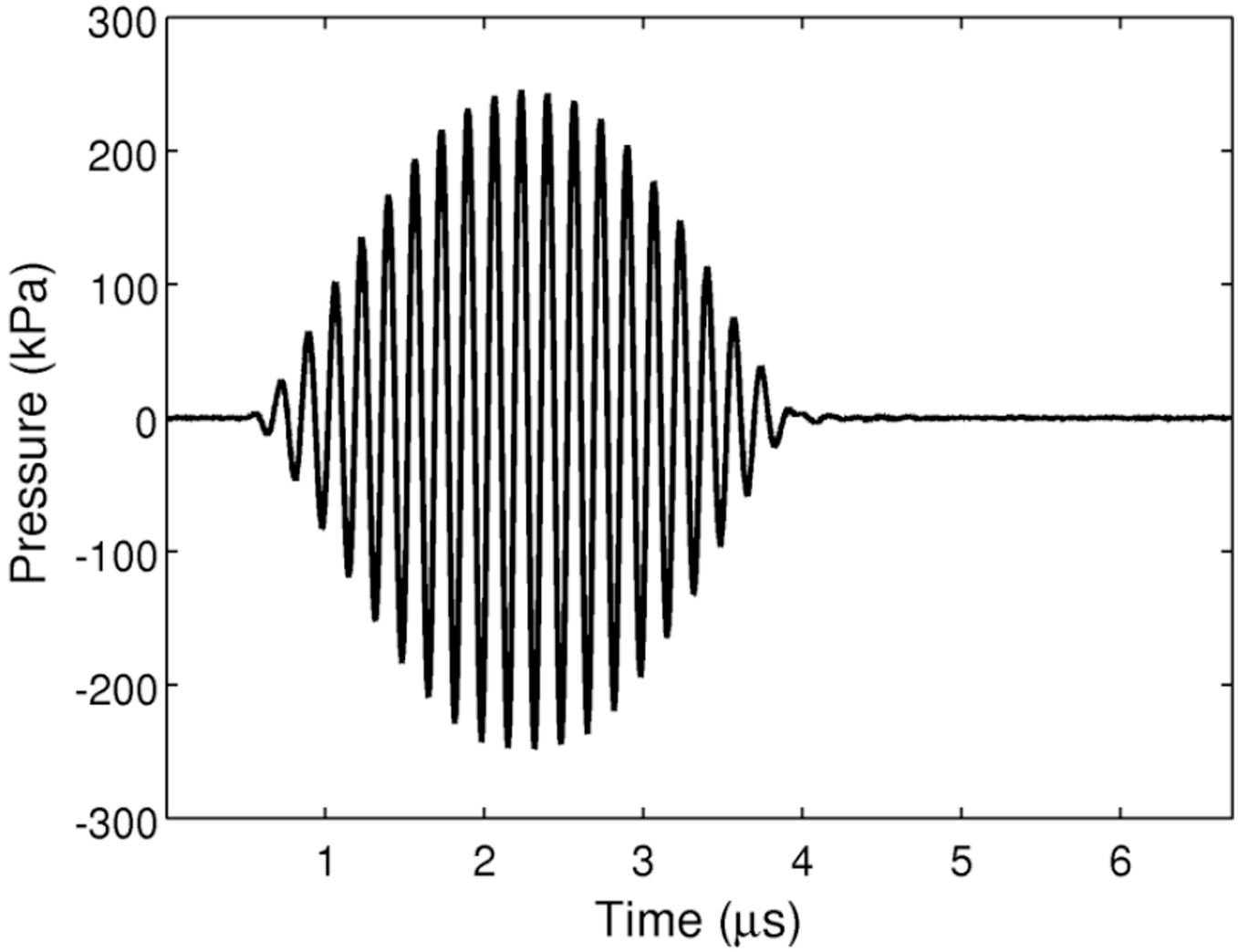

Figure 2.

Measured pressure waveform for a 250 kPa acoustic excitation. A 3.33 μs tone burst excitation consisted of a 20-cycle sinusoidal wave with a cosine envelope and a fundamental frequency of 6 MHz. The time axis limits were chosen to indicate the temporal timing of the pulse with respect to the duration of a typical recording acquired using ultra-high-speed framing camera commencing at time t = 0 and consisting of 128 frames captured at approximately 19×10^6 frames per second.

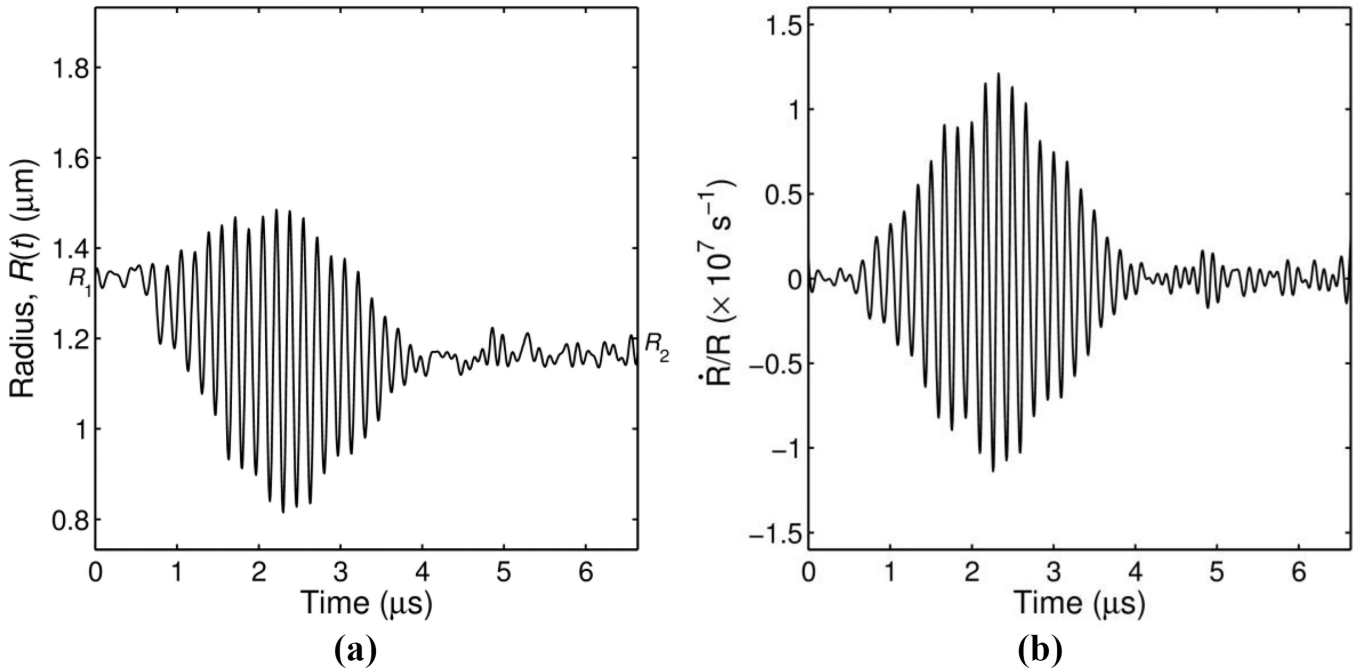

Figure 3.

(a) Example of a measured radius versus time curve and **(b)** dilatation rate calculated for a microbubble excited by a single ultrasound burst at peak pressure of 110 kPa. The initial radius is R_1 = 1.33 μm and the final radius is R_2 = 1.17 μm.

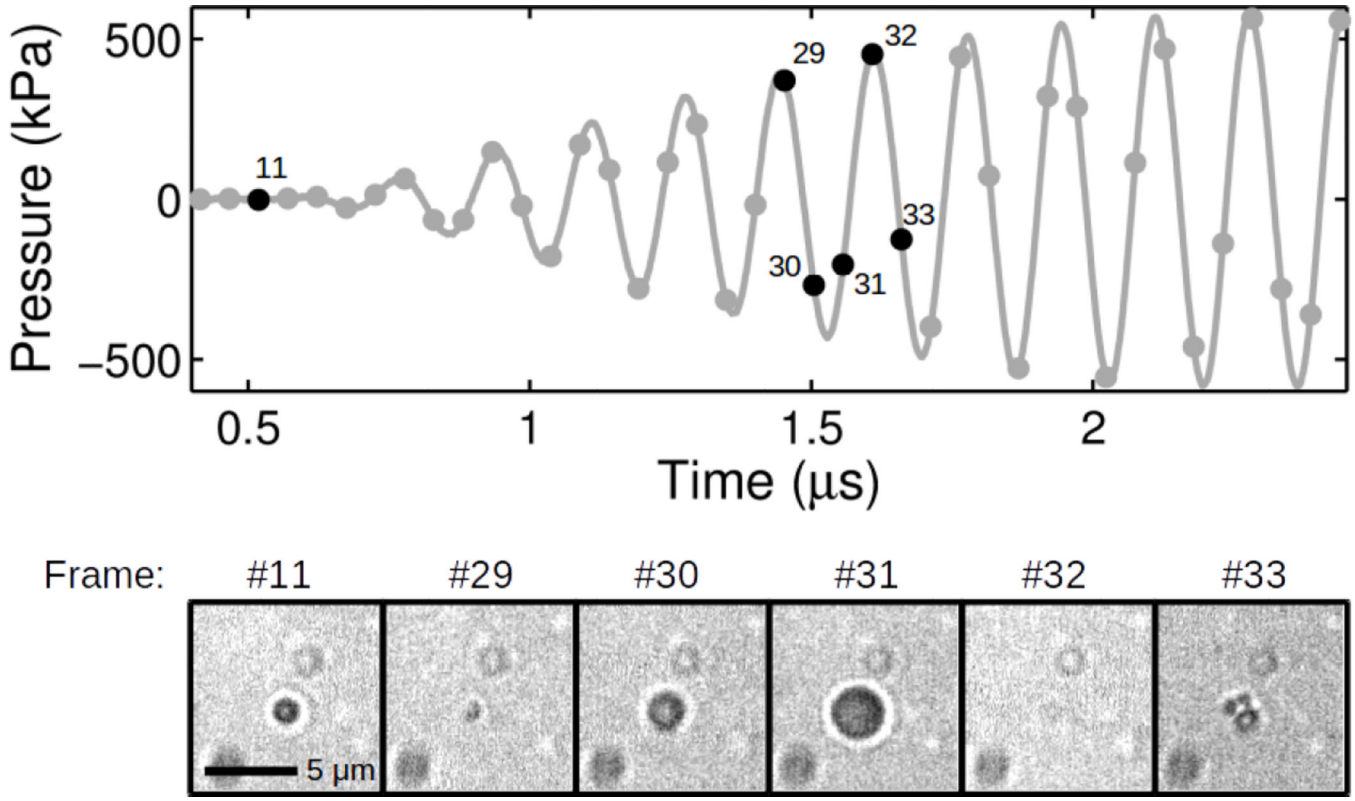

Figure 4.

Exemplary ultra-high-speed image frames for an echogenic liposome fragmenting. Frames #11 and #29 – #32 are shown in the bottom panel. The top panel shows the temporal location of each image frame (*black dots*) with respect to the acoustic driving pressure. The scale bar represents 5 μm in the images and the interframe time is 52 ns.

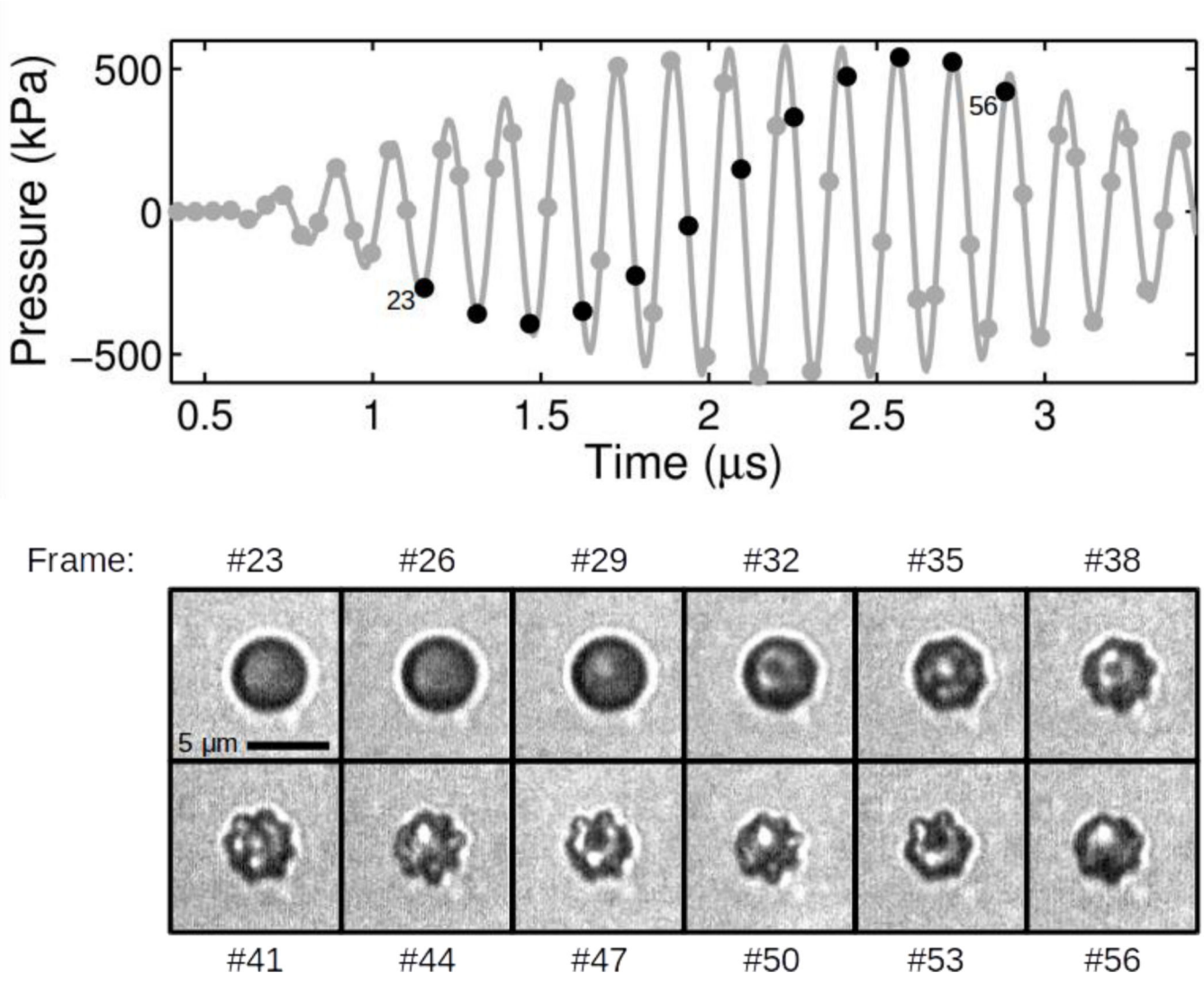

Figure 5.

Exemplary ultra-high-speed image frames for an echogenic liposome with radius variations and patterns indicative of surface mode oscillations. Each third frame from #23-#56 is shown in the bottom panel. The top panel shows the temporal location of each image frame (black dots) with respect to the acoustic driving pressure. The scale bar represents 5 μ m in the images and the selected frames are separated by 0.157 μs.

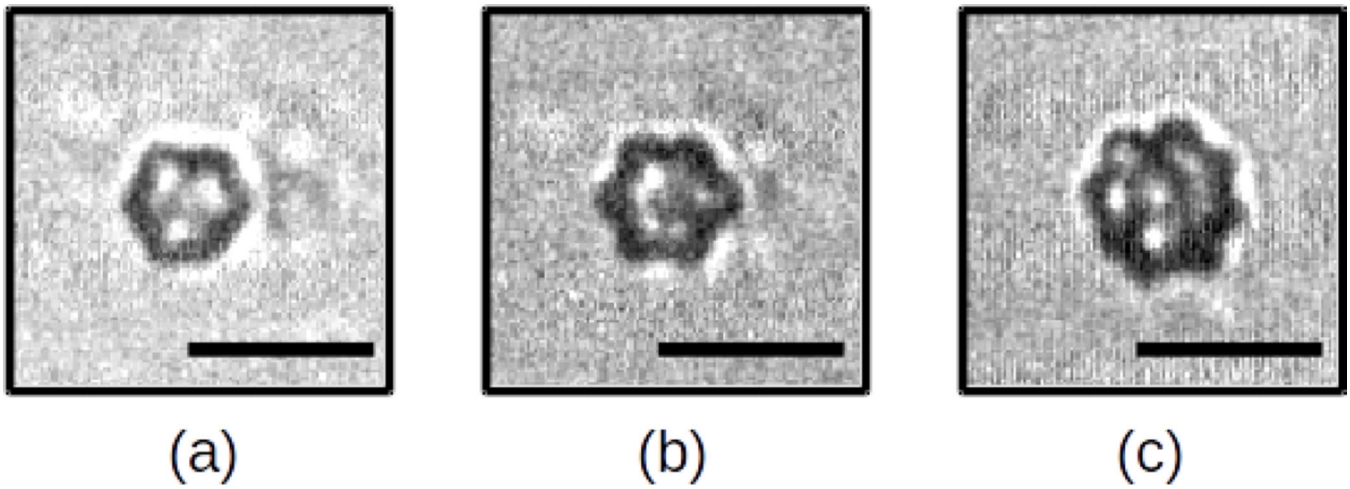

Figure 6.

Examples of asymmetric patterns indicative of surface mode vibrations observed for ELIP with initial radii of **(a)** 1.8 μ m **(b)** 2.0 μ m and **(c)** 2.2 μ m. The peak pressure amplitude was 410 kPa in (a,b) and 580 kPa in (c). Scale bars represent 5 μ m in all images.

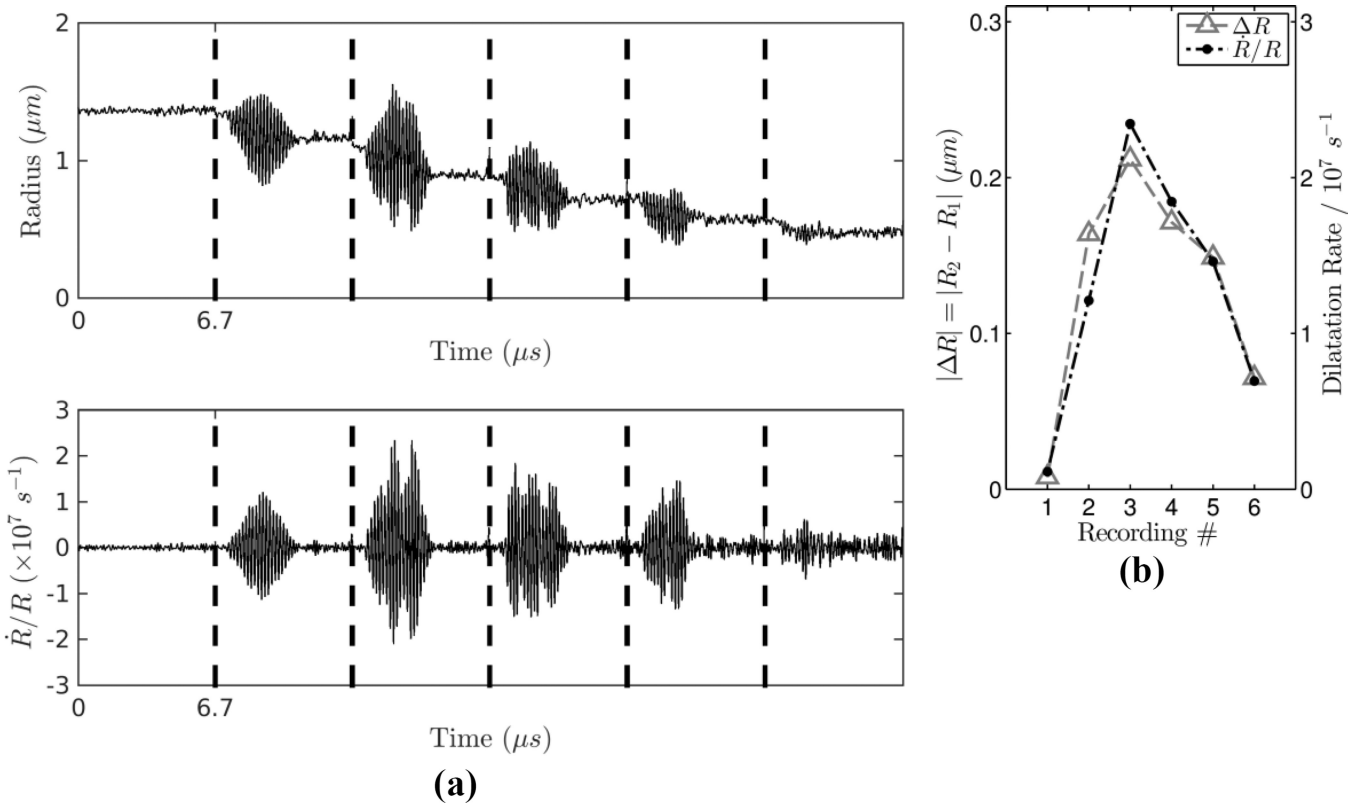

Figure 7.

(a) Example radius versus time sequence (top) and dilatation rate (bottom) derived from 6 successive optical recordings for a single ELIP. The duration of each recording is 6.7 μs and the dotted lines between recordings represent ~80 ms delay due to CCD readout and transfer to memory. **(b)** Absolute change in radius and maximum dilatation rate derived from each of the recordings.

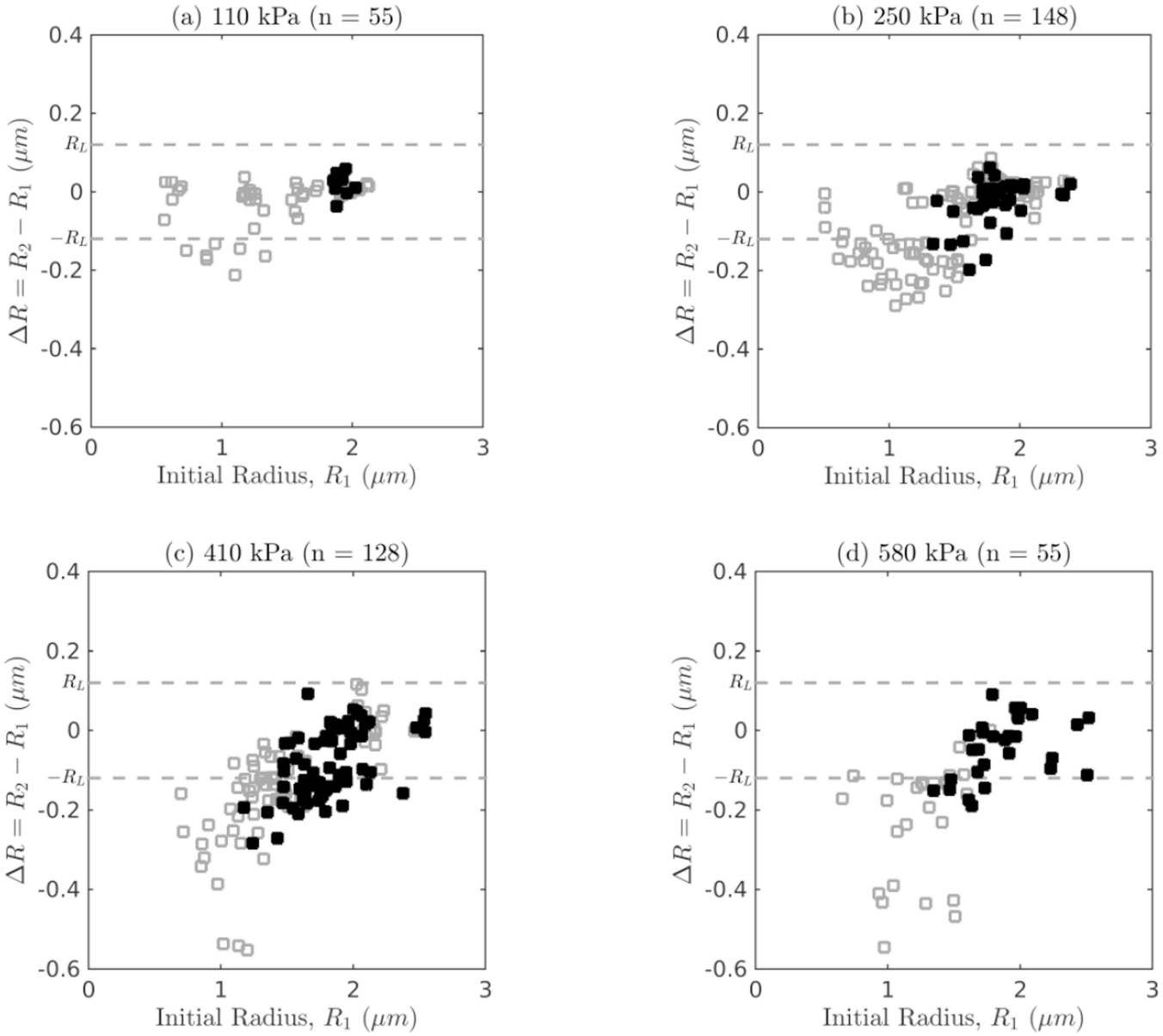

Figure 8.

Change in radius versus initial size for a single burst at **(a)** 110 kPa, **(b)** 250 kPa, **(c)** 410 kPa, and **(d)** 580 kPa. The filled symbols denote trials in which surface modes were observed. The resolution limit for a detectable change in radius, R_L, is plotted as a dashed line.

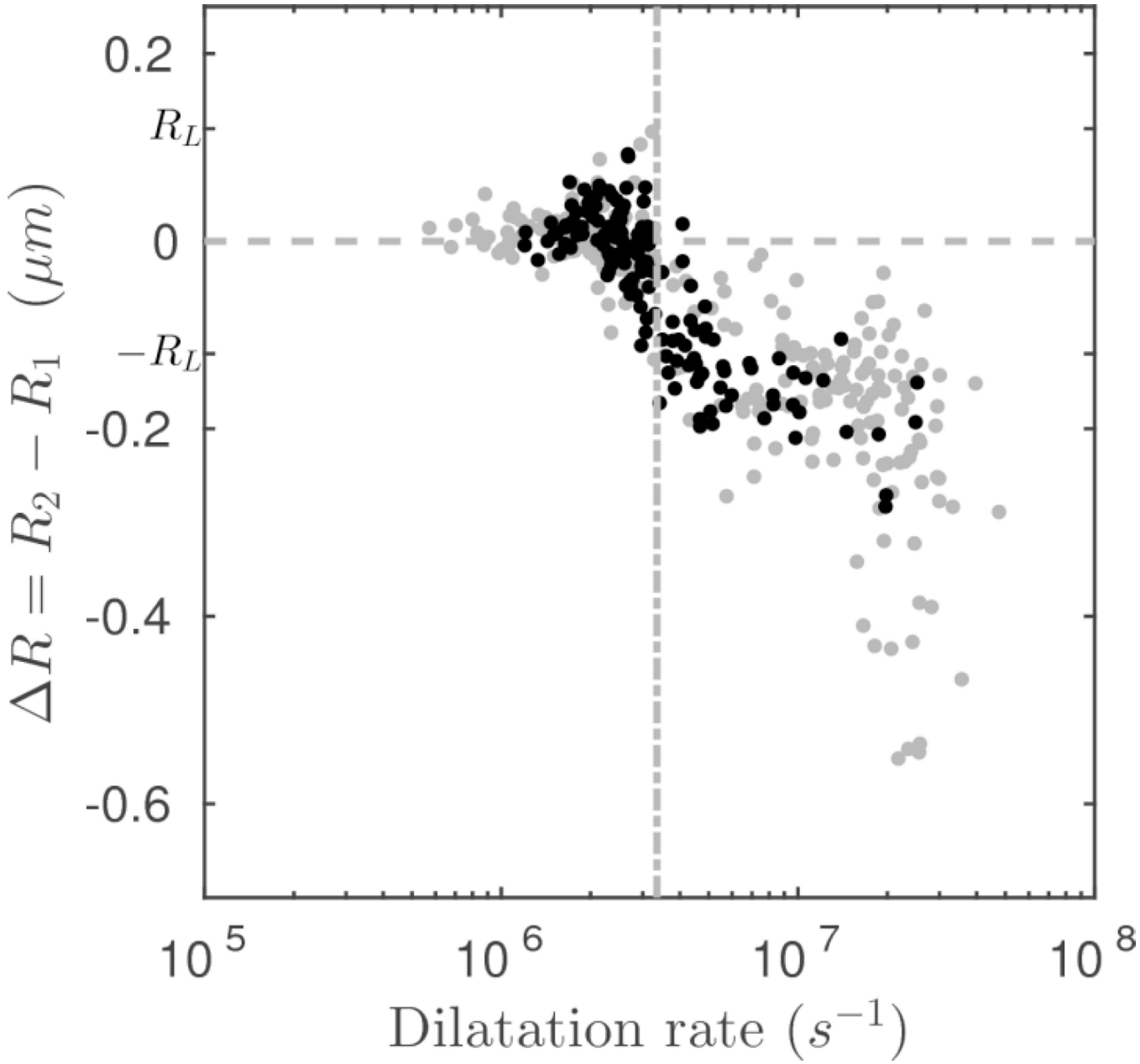

Figure 9.

Change in radius versus dilatation rate. The change point was evaluated using the mean square error (MSE) estimator and is shown as a dashed line at 3.4×10^6 s^{-1}. The filled symbols denote trials in which surface modes were observed.

Table 1

Initial radius and maximum expansion ratio for ELIP observed to fragment.

	R_1 (μm)	R_{max} / R_1
410 kPa	0.94	1.52
	0.99	1.60
	L.00	1.60
	L.01	1.82
	1.03	1.60
580 kPa	0.75	1.95
	0.85	1.77
	1.01	1.71
	1.03	2.24
	1.04	1.46
	1.05	1.53

Table 2

Observations of surface mode vibrations for each peak pressure level.

	110 kPa	250 kPa	410 kPa	580 kPa
$R_1 < 1.5\ \mu m$	0/25 (0%)	4/53 (8%)	9/51 (18%)	3/23 (13%)
$R_1 \geq 1.5\ \mu m$	8/30 (27%)	40/95 (42%)	56/77 (73%)	27/32 (84%)
Total	8/55 (15%)	44/148 (30%)	65/128 (51%)	30/55 (55%)